

ARTICLE TYPE**Scales of Stability and Turbulence in the Molecular ISM**

Eric Keto

¹Institute for Theory and Computation,
Harvard University, Cambridge, MA, USA**Correspondence**

Eric Keto

Present AddressCenter for Astrophysics, 60 Garden St,
Cambridge, MA 02138**Abstract**

We re-analyze the data of the BU-FCRAO ¹³CO Galactic Ring Survey (GRS) to understand the dynamics of the turbulent molecular interstellar medium. We define molecular clouds by their spatial half-power contours of ¹³CO integrated intensity, independent of a boundary based on thresholding or tiling. We find properties of hydrostatic equilibrium (HE) and virial equilibrium (VE), the former independent and the latter dependent on time and spatial scales. We suggest that HE is a stationary property of the turbulence and that molecular clouds are high-density regions of a fluctuating component. The gravitational and turbulent kinetic energies within clouds are continuously evolving toward a time-dependent VE with the fluctuating, external, turbulent pressure energy (PE) that can be treated parametrically owing to the shorter time scale for virialization. The average PE is comparable to the pressure of the multiphase ISM at the Galactic mid-plane. Larson's scaling relations analyzed by different statistical methods are not significant. The non-dimensional variances of size, line width, and column density are of comparable magnitude, ruling out the inference of constant column density. Previously unrecognized autocorrelations may have contributed to the apparent validity of the inference.

KEYWORDS:

Interstellar Medium, Molecular Clouds, Turbulence, Virial Equilibrium

1 | INTRODUCTION

The Boston University-Five College Radio Astronomy (BU-FCRAO) Galactic Ring Survey (GRS) images 75.4 square degrees of the first Galactic quadrant in ¹³CO spectra with 46" angular resolution and Nyquist sampling on a 22" grid (Jackson et al., 2006). Over 6000 molecular clouds¹ are identified in the survey (Rathborne et al., 2009) with kinematic distances (Roman-Duval et al., 2009) that enable conversion of the basic cloud properties to dimensions of length, mass, and energy (Roman-Duval, Jackson, Heyer, Rathborne, & Simon, 2010).

All the clouds are at least partially resolved by the design of the segmentation algorithm used in Rathborne et al. (2009) for cloud identification. The low observational noise

($\sigma_{T_A} \sim 0.13$ K) and Nyquist sampling reveal ¹³CO emission extended many times the cataloged radii around the clouds. From the ¹³CO integrated intensity and the line width, proportional to the column density and the turbulent velocity dispersion, respectively, we develop an observational description of the gravitational potential energy (GE) and turbulent kinetic energy (KE) within the clouds and throughout the surrounding molecular interstellar medium (ISM). This paper presents the results of our new analysis of the GRS data.

In agreement with previous results of other surveys (Evans, Heyer, Miville-Deschênes, Nguyen-Luong, & Merello, 2021; Heyer, Krawczyk, Duval, & Jackson, 2009; Miville-Deschênes, Murray, & Lee, 2017) we find that the KE and GE per unit mass are correlated with an excess of KE. We find that $\langle 2KE \rangle / \langle GE \rangle \sim 2.2$, and that the turbulent pressure energy per unit mass of the more diffuse molecular ISM around each cloud, estimated from the square of the ¹³CO line widths,

¹Rathborne, Johnson, Jackson, Shah, and Simon (2009) define clouds as complexes of clumps within a spatial and velocity range. We refer to all identifications as clouds. Our definition of a cloud is explained more fully in §2 and §3.

$PE = \sigma^2$, is sufficient to complete the virial equilibrium, $PE \sim 2KE - |GE|$. These results add to the observational evidence for the appearance of stability in the molecular ISM.

Turbulence is pervasive on all scales in the molecular ISM. Because regions of dynamical equilibrium generally do not exist within fully developed turbulence (Klessen, Ballesteros-Paredes, Vázquez-Semadeni, & Durán-Rojas, 2005; Vázquez-Semadeni, 1998), these observations of stability seem at odds with theories of molecular clouds as turbulent eddies or compressed regions between colliding flows (Elmegreen, 1993; Mac Low & Klessen, 2004). Why the clouds appear to be in virial equilibrium has not been explained.

This paper suggests that the resolution of the paradox of virial equilibrium within turbulence is found by consideration of the different time scales for the evolution of the three terms for energy KE, GE, and PE. The dynamical time scale for the turbulence at any scale is approximately its crossing time or eddy turnover time, $T_x = R/\sigma$ (Gammie & Ostriker, 1996; Kolmogorov, 1941). If the turbulent velocity dispersion, σ , scales with a power of the length scale, R , less than one (Heyer et al., 2009; Padoan, 1995), then the turbulence on smaller spatial scales evolves with a shorter time scale than on longer spatial scales.

The rate of virialization within a cloud is then more rapid than the rate of change of the external PE due to turbulent fluctuations around the cloud. In the snapshot in time represented by an observation, the clouds are in a time-dependent, continuously evolving virial equilibrium within a more slowly evolving external pressure that can be considered parametrically in the virial theorem applied to each cloud.

In section §4.6, we consider the two empirical scaling relations between cloud size, line width, and column density proposed by Larson (1981), possibly indicative of properties of the turbulent, molecular ISM (Kritsuk, Lee, & Norman, 2013). Our results generally confirm the previous GRS study of Heyer et al. (2009). Additionally, we evaluate the statistical significance by comparing the mean square errors of the regressions of the cloud properties with their variances and find that neither correlation is significant. A comparison of the variances in non-dimensional units shows that the independence of column density and cloud size cannot be interpreted as implying constant column density. Rather the two quantities have uncorrelated log normal distributions.

In §4.7, we define a complexity parameter to measure the departure from the circular shape expected for a cloud in the spherical minimum-energy configuration of hydrostatic equilibrium. We find 90% of the clouds have shapes inconsistent with hydrostatic equilibrium.

In §4.8, we compare the column density probability distribution functions (PDF) inside and outside the clouds. Both are close to log normal.

The Discussion §5 suggests that the conditions in the molecular ISM, as described by the GRS, are suitable for the growth and fragmentation of molecular clouds by a turbulent cooling instability (Keto, Field, & Blackman, 2020).

2 | DEFINITIONS

We consider molecular clouds and the virial theorem differently than many previous observational studies. This section explains the definitions of molecular clouds, cloud size, and time-dependent equilibrium.

2.1 | Definition of a Molecular Cloud

We define a cloud as a region of higher column density identified by a peak in the ^{13}CO integrated intensity that is at least twice the level of the azimuthally-averaged intensity around the peak. This defines a cloud outward from its center without reference to a boundary specified as an intensity threshold or as a tiling from a segmentation algorithm. Higher-density regions within larger clouds (sometimes called clumps) are identifiable with the same definition applied to any local peaks and their surrounding intensities. We refer to all over-densities meeting our definition simply as clouds.

2.2 | Definition of the Cloud Size or Radius

We define a characteristic length (radius) for each cloud as twice the HWHM of the radial intensity profile azimuthally averaged around the peak. The motivation for the factor of two follows from the power-law density structure of an idealized cloud described by the Lane-Emden equation. Similar to the description of an exponential curve, we identify an outer region in the density profile that may be approximated as linear with respect to an inner non-linear region where the density profile rises steeply. The break point occurs at approximately 2 HWHM. The properties of the molecular ISM are continuous across the defined radius (§4.1).

We use the length scale of the cloud to separate the length scales of the turbulence into the smaller scales inside the cloud and the larger scales outside. Results of the analyses that depend on this separation, for example virial equilibrium in an external pressure, are not sensitive to the exact definition of the length scale owing to the scale-free nature of turbulence and the continuity of properties within the molecular ISM (§4.3).

2.3 | Definition of Time-dependent Virial Equilibrium

The time-dependent virial theorem in units of energy per unit mass including an external pressure (Field, Blackman, & Keto, 2011; Spitzer, 1978) is,

$$\delta(t) = \sigma(t)^2 - \Gamma \Sigma(t) R(t) - \sigma^2(R(t), t)/3 \quad (1)$$

where $\Sigma(t)$ is the column density, $\sigma(t)$ is the velocity dispersion, both as averages within the cloud, and $\sigma^2(R(t), t)/3$ is the external PE per unit mass, P_e/ρ , due to the turbulence at the outside boundary of the cloud, $R(t)$, with ρ the average mass density within the cloud. The constant, $\Gamma = 4\pi\beta G/3$, and β depends on the density distribution within the cloud, $3/5$ for uniform or 0.732 for hydrostatic used here. With a Lagrangian interpretation, the mass, M , is constant while the other variables depend on time. Here $\delta(t)$ is a measure of disequilibrium at time t .

Because we lack observational data on the magnetic field energies in the GRS clouds, a separate term for the magnetic energy is not included in equation 1. To the level of accuracy of our observational analysis, one could assume that the turbulent magnetic energy is in equipartition with the observed KE. In this case, the external pressure energy derived from the GRS data (§4.2) would be higher by less than a factor of 2.

3 | METHODS

This section on methods describes the procedures to select the subset of clouds suitable for analysis, to co-add radial profiles across different length scales, and to calculate the cloud properties such as column density, line width, and external PE. Readers more interested in the results may proceed to §4 and refer back here as necessary.

3.1 | Identification of the Clouds

We rely on the positions and velocities in the catalogs of Rathborne et al. (2009) for preliminary identification of individual clouds. Not all the clouds are suitable for our analysis.

We define the following filters:

- (1) No distance. Not all the clouds in the catalog of Rathborne et al. (2009) have an estimated distance in the catalog of Roman-Duval et al. (2009).
- (2) Overlapping spectral lines. Clouds with spectral lines that overlap within the spectral HWHM of the VLSR are rejected. Individual spectral lines are identified by a peak-finding algorithm that traverses the spectrum and identifies a separate spectral line as a local peak that is five times the local noise level above the last local minimum.

- (3) Duplicate identification. Two clouds that have peak integrated intensities within $3/4$ of the survey angular resolution and VLSRs within each other's line widths are the same cloud.
- (4) Peak integrated intensity below $1 \text{ K km s}^{-1} \text{ pixel}^{-1}$ ($S/N < \sim 7$). While a peak may be identifiable, the intensities off-peak are too low for our analysis.

- (5) No half-power width. The peak intensity might not be above twice the level of the surroundings; or, the radial profile might be too complex.

- (6) Confusion with another cloud. If a local intensity peak is located within another cloud whose emission is steeply rising in one direction, the peak may have a half-power level, but the majority of pixels within the HWHM may have intensities above the peak or a single pixel may have an intensity more than 1.5 times the peak.

(1) Number of clouds missing a distance: 357

(2) Number of clouds with overlapping spectral lines: 257

(3) Number of clouds with duplicate identifications: 878

(4) Number of clouds with peak integrated intensity $< 1 \text{ K}$: 229

(5) Number of clouds with no half-power point: 402

(6) Number of clouds with confusion: 170

Number of clouds selected for analysis: 4190 out of 6155.

Some clouds are rejected for more than one reason.

3.2 | Properties of Individual Clouds

Previous studies of the GRS data (Heyer et al., 2009; Roman-Duval et al., 2010) derived the molecular gas column densities from ^{13}CO and ^{12}CO excitation temperatures to minimize optical depth effects. They used the ^{12}CO data from the earlier University of Massachusetts-Stony Brook Galactic Plane Survey (UMSB) (Solomon, Rivolo, Barrett, & Yahil, 1987). We find that we can reliably match the column densities in (Heyer et al., 2009) with the ^{13}CO conversion factor of $22 \text{ M}_\odot \text{ pc}^{-2} / \text{K km s}^{-1} \text{ pc}^2$, suggested in Phiri, Kirk, Ward-Thompson, Sansom, and Bendo (2021). We compute the spectral line width from the second moment of the ^{13}CO spectral line.

We calculate the column density and line width for each pixel in a 128×128 pixel box (96×96 arc minutes) around the peak integrated intensity of each cloud. Pixels with intensity less than five times the observational noise are ignored. The column density and velocity dispersion of a cloud are taken to be the averages, respectively, of the quantities per pixel within a circular radius of 2 HWHM (§2.2) around the peak. The mass is the sum of the column densities per pixel.

3.3 | Co-added Radial Profiles

The radial profiles of the ^{13}CO integrated intensity and line width of individual clouds can be co-added by scaling the

lengths of both profiles by the HWHM of the column density profile and normalizing their respective line intensities or line widths. The variation of the line width per pixel is noisier than that of the intensity, so for the purpose of normalization, we define the line width at the cloud center as the average line width within half the HWHM.

There is often emission from more than one cloud within our 128×128 pixel analysis box around each cloud and within the spectral window ($\text{VLSR}_{\text{cloud}} \pm \text{FWHM}$). This emission is included in the azimuthal averaging of the radial profiles for the individual clouds (§4.2). Because azimuthal averaging is inherent in our definition of a cloud, the effect of a nearby cloud on the gradients is diluted by the fraction of its angular intercept and by the separation squared. For the calculation of the sample-average radial profiles, we exclude clouds whose radial profiles are strongly affected by other clouds. We exclude 507 clouds with profiles where the normalized intensity exceeds 0.4 beyond 3 HWHM. The co-added average profiles include 3683 clouds.

The observed azimuthally-averaged radial profiles around the individual clouds extend to the boundaries of our analysis box around each cloud, 48 arc minutes, regardless of the size of the cloud. Clouds with larger HWHM measured in arc minutes do not extend as far in non-dimensional units as those around smaller clouds. Thus the averaging at large non-dimensional radii includes fewer clouds and the average profile becomes noisier with distance. After rescaling and co-adding we have good data out to a non-dimensional radius of 20 HWHM.

4 | RESULTS

4.1 | Radial Profiles of Individual Clouds

Figure 1 shows radial profiles of column density for 30 example clouds in three groups of ten for smaller, medium-sized, and larger clouds with respect to each other. The profiles are normalized to units of the HWHM (§3.3). Comparison shows that for clouds of all sizes, our arbitrary definition of the cloud length scale at 2 HWHM (§2.2) is a reasonable division between the steeply rising column densities within the clouds and the flatter surrounding column densities although the profiles are continuous. The profiles appear to indicate approximate hydrostatic equilibrium (§4.3) with random perturbations that can be ascribed to turbulence.

4.2 | Properties of the Individual Clouds

Figure 2 shows histograms of the three variables, the radius, line width, and column density and their best-fit log normal functions with means and standard deviations listed in table 1. The median values of our cloud properties are listed in table

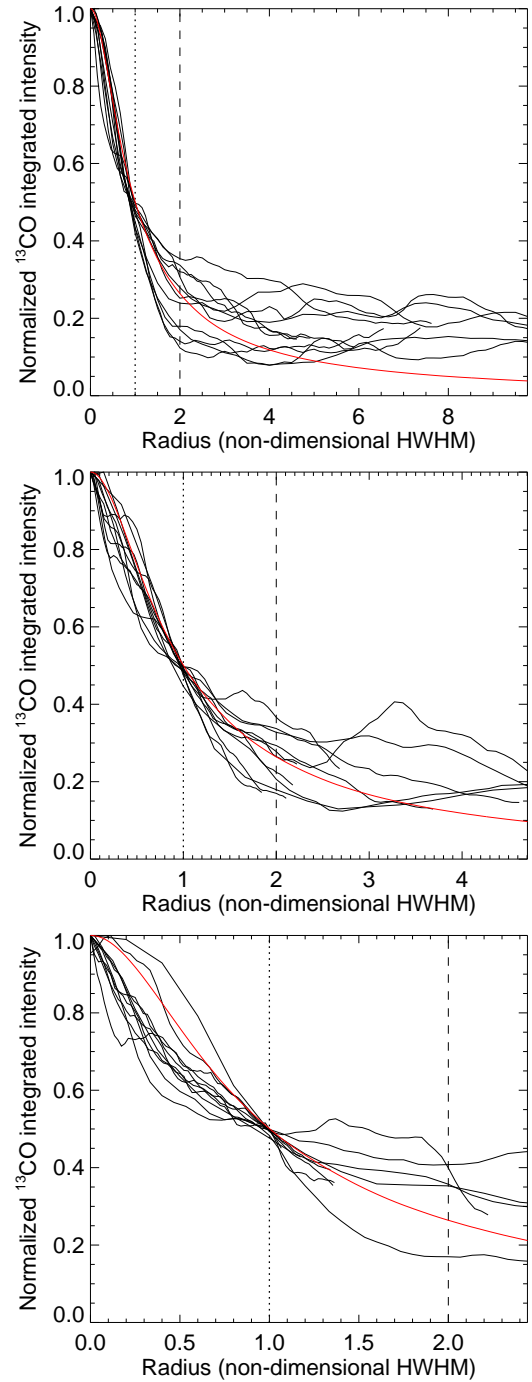


FIGURE 1 Thirty individual azimuthally-averaged radial profiles of ^{13}CO integrated intensity ($\text{K km s}^{-1} \text{ pixel}^{-1}$). *Top to bottom* show 10 profiles each for clouds that have small, medium, and large sizes with respect to each other. The vertical, dotted and long-dashed lines indicate the HWHM and the length scale of the cloud defined as 2 HWHM. The red line shows the column density of hydrostatic equilibrium (§4.3), same as in figure 4 (*right*, blue, long-dashed line).

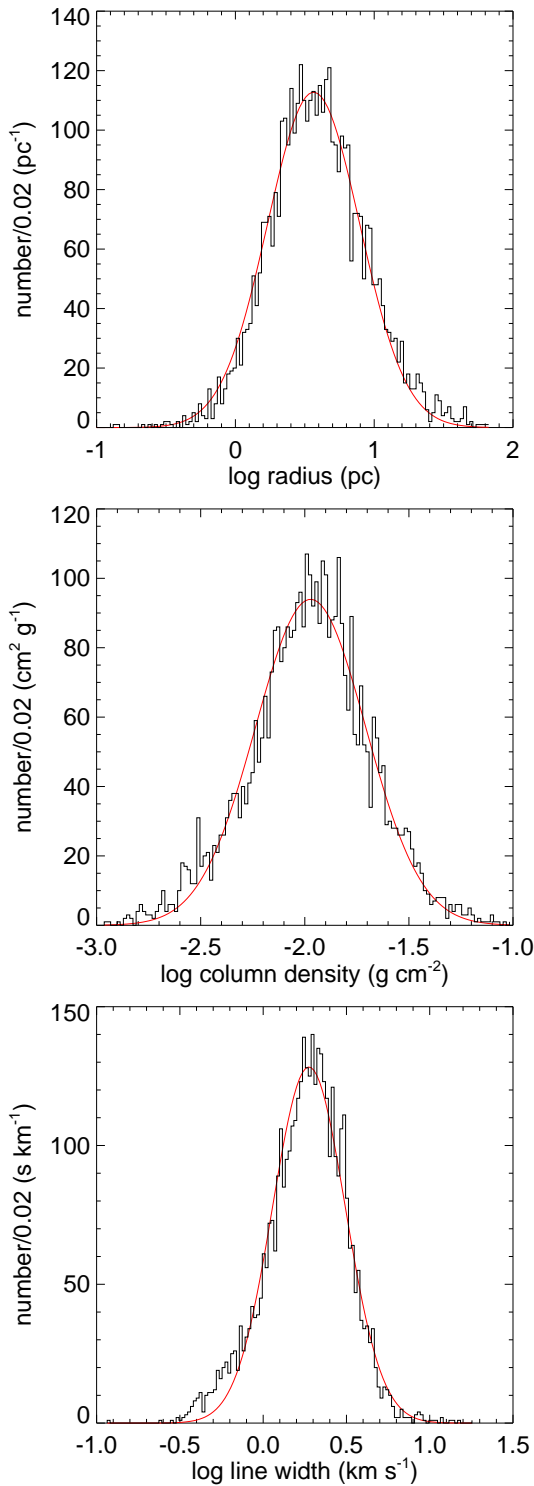


FIGURE 2 Histograms showing the log normal distributions of radius, column density, line width. Means and standard deviations are listed in table 1 .

2 along with those calculated from the catalogs of Rathborne et al. (2009) following the same procedure we use to convert observational to physical units but with their clouds defined by their segmentation.

The median radii of our clouds are larger than those in Rathborne et al. (2009), while the median column densities and velocity dispersions are the same. The segmentation algorithm used in Rathborne et al. (2009) tiles the emission into clouds that intersect only on their boundaries. A cloud with multiple intensity peaks may be tiled into smaller clouds around each peak. Our clouds, defined to study the continuous gradients of column density and turbulent energy, would, by comparison, extend across these truncations imposed by the tiling to result in overlapping clouds that share pixels.

4.3 | An Average Hydrostatic Equilibrium Across the Scales of Turbulence

Most of the clouds have ^{13}CO line widths per pixel that are lower in the cloud centers and lower than in the surrounding gas. This can be seen in two ways: in maps of the spectral line width and in the sample-average radial profile of the line width.

Figure 3 shows pairs of maps for several clouds. The map on the left is the ^{13}CO integrated intensity ($\text{K km s}^{-1} \text{ pixel}^{-1}$) that is proportional to the column density after accounting for distance. The map on the right shows the spectral line width (km s^{-1}). The pairs show a negative correlation between the column density and the line width.

Not all the individual clouds in the survey show a negative correlation², but most do as can be seen in figure 4 that shows the non-dimensional, sample-average radial profile of the line width from 3683 clouds (§3.3).

From the minimum value at the beginning of the profile ($R = 0$) to the maximum value at the end ($R = 20$ HWHM), the line width increases by 40%. About half the increase occurs within the cloud.

The corresponding sample-average radial profile of the ^{13}CO integrated intensity, figure 4, also shows a continuous relationship between the cloud and its surroundings. Two column densities from the Lane-Emden equation for hydrostatic equilibrium are included for comparison. The dotted line shows the profile with a constant non-dimensional temperature. The long-dashed line shows the profile with the non-dimensional temperature proportional to the square of the sample-average radial profile line width (figure 4 left), proportional to the turbulent energy. There is no statistical reason

²Regions of active star formation, associated with high column densities, may show larger line widths than quiescent regions due to feedback processes such as bipolar outflows and HII regions. Observations of specific molecular clouds from the literature may not be representative of all molecular clouds because observations of active regions are over-represented compared to quiescent regions due to selection bias in favor of astrophysically interesting observational targets.

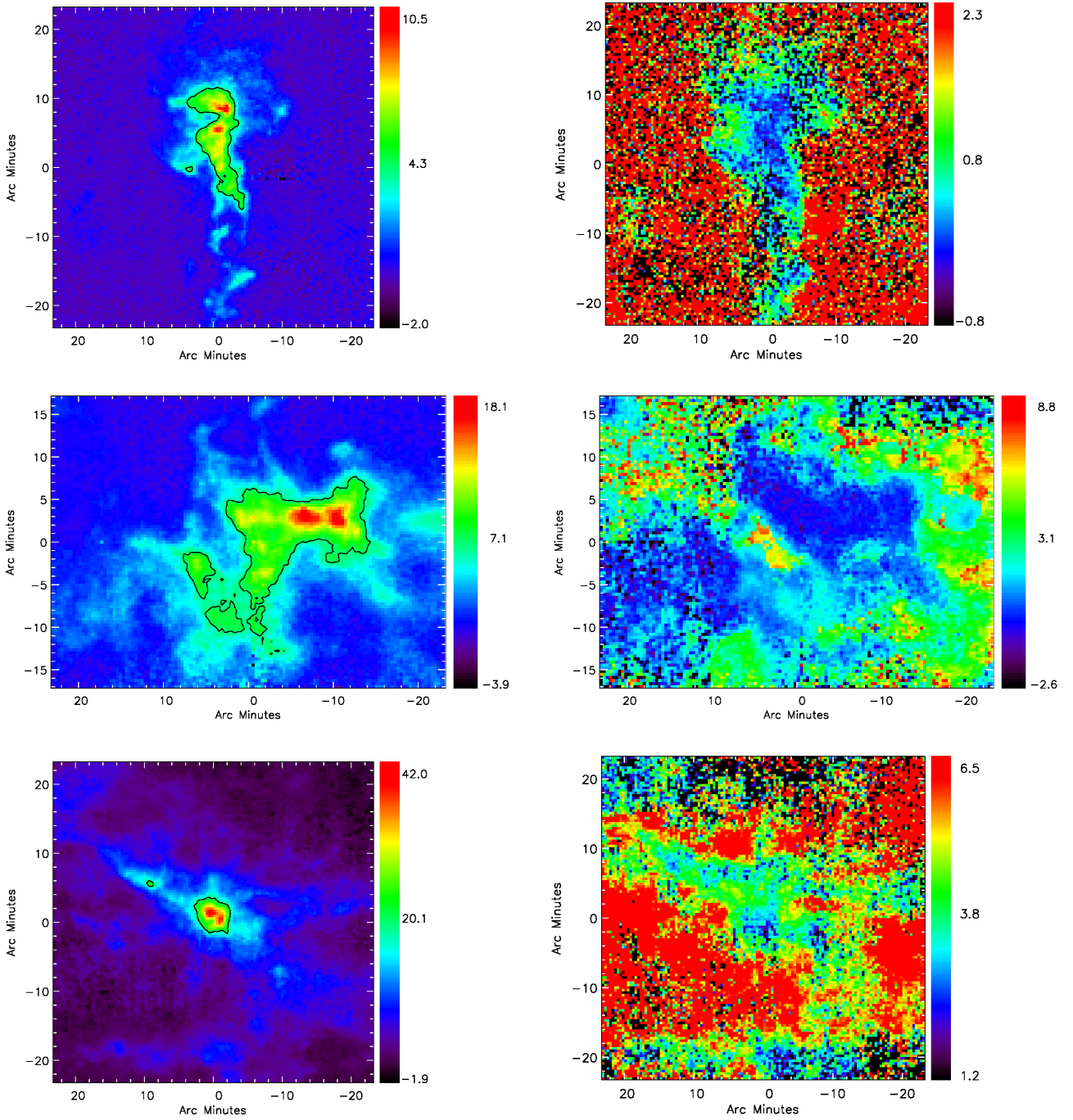


FIGURE 3 (*Left*) The ^{13}CO integrated intensity ($\text{K km s}^{-1} \text{ pixel}^{-1}$) and (*right*) line width (km s^{-1}) with a color bar indicating the values in these units, respectively. From *top to bottom*, the clouds shown are clumps 54, 64, and 70 from the clumps catalog of Rathborne et al. (2009). The single contour (*left*) is drawn at the half-power level of the peak integrated intensity within the contour. The cloud length scale is twice the circularly averaged HWHM.

why the individual profiles should average to the solution of the Lane-Emden equation so precisely as in figure 4.

The interpretation of average hydrostatic equilibrium in the molecular ISM requires consideration. The Nyquist sampling

of the GRS ensures that the data include the full range of accessible spatial scales from the limit of the angular resolution at 46 arc seconds to the maximum extent of the radial profiles at

48 arc minutes. The two average radial profiles are then averages across all spatial scales. On average, the turbulence on any scale is in hydrostatic equilibrium with the scales above and below. On average, the turbulent molecular ISM is neither collapsing nor expanding on any scale. This is consistent with the low efficiency of star formation. At any time, only a small fraction, 0.6%, of the molecular ISM is gravitationally collapsing to form stars (Evans et al., 2021).

Because of the relationship between the turbulent dynamical time scale and the spatial scale, we can think of the averaging across spatial scales as an averaging across dynamical time scales. Therefore, the property of average hydrostatic equilibrium is a stationary or time-independent property of the turbulence. Because this property applies on all scales including the length scale of each molecular cloud, there is a stationary component of hydrostatic equilibrium in each cloud as well (figure 1).

The molecular ISM between clouds should also be in approximate hydrostatic equilibrium. As the distance increases from the concentration of mass in a molecular cloud, the hydrostatic equilibrium becomes dominated by pressure balance.

4.4 | Virial Equilibrium in Pressure

Figure 5 shows a 2-D histogram of 4190 GRS clouds (§3.1) in the plane of the KE vs. GE, both per unit mass, and the number of clouds in bins of $(0.05 \text{ km}^2 \text{ s}^{-2})^2$ in color. The parameters of a 2-D Gaussian fit to the distribution are given in table 3. An ellipse is shown with position angle 49° and with semiaxes respectively equal to the variances of the energies, 0.06 and $0.02 \text{ km}^2 \text{ s}^{-2}$. In the 2-D space of energy, the clouds are clustered in this elliptical distribution whose major axis is approximately aligned with the 45° straight line of virial equilibrium with a constant PE per unit mass (equation 1), $P_e = 1.17 \pm 0.16 \text{ km}^2 \text{ s}^{-2}$.

The local, external PE can also be measured directly from the observed azimuthally-averaged line width at the cloud boundary, $\sigma^2(R)$ (equation 1). The measure of virial disequilibrium (equation 1), $\delta = -0.97 \pm 13.76 \text{ km}^2 \text{ s}^{-2}$. The distribution of δ shown in figure 6 indicates that the difference from zero is not significant. Thus the energies of the individual clouds are in time-dependent virial equilibrium with their local external PE estimated directly from the ^{13}CO line widths around the clouds.

The elliptical distribution of the KE and GE is a property of the fluctuating component of the turbulence. The alignment of the major axis indicates a preference for combinations of KE and GE that satisfy virial equilibrium with external pressures given by equation 1 and figure 6. A standard population-lifetime argument then suggests that the clouds are able to

evolve toward virial equilibrium faster than the larger scale fluctuations in the turbulence perturb them out of equilibrium.

4.5 | External Pressure

The comparable variability of the PE outside the clouds and the KE and GE inside the clouds (§4.4), suggests that the external PE is due turbulent fluctuations in the molecular ISM on scales larger than the clouds. In figure 1, the perturbations from hydrostatic equilibrium at and beyond the cloud radius (2 HWHM) contribute to the variability of the confining external PE.

In units of energy per volume, the elliptical distribution has semiaxes of 0.78 and $0.21 \text{ ergs cm}^{-3}$, and the average external pressure, $P_e = 2.12 \pm 1.96 \times 10^4 k_B \text{ K cm}^{-3}$. This pressure is comparable to estimates of the pressure of the ISM at the mid-plane of the Galaxy, $\sim 1 \times 10^4 k_B \text{ K cm}^{-3}$ (Bloemen, 1987; Boulares & Cox, 1990; Elmegreen, 1989). The average external pressure represented by the solid line in figure 5 may be a stationary property of the turbulent molecular ISM that is imposed as an outer boundary condition by the pressure of the multi-phase ISM.

4.6 | Larson's Laws

Based on data from the early days of radio frequency spectral line observations, Larson (1981) proposed that the line width and number density averaged within molecular clouds scale with the cloud length, L , as $\sigma \propto L^{0.38}$ and $n \propto L^{-1.10}$, respectively, over 3 orders of magnitude in length. The two relationships straddle the dichotomy between turbulence and stability in the ISM. Turbulence is indicated by the exponent of the first scaling relationship, between $1/3$ consistent with incompressible turbulence and $1/2$ consistent with compressible turbulence (Kritsuk et al., 2013; Padoan, 1995). Stability is indicated by second scaling relationship because virial equilibrium would be implied if the exponent of the first scaling relationship were actually $1/2$ and the column density " $nL \sim \text{constant}$ " (Larson, 1981). The validity of these scaling relations has been questioned on various grounds (e.g. Ballesteros-Paredes, Román-Zúñiga, Salomé, Zamora-Avilés, and Jiménez-Donaire (2019); Scalo (1990); Vázquez-Semadeni, Ballesteros-Paredes, and Rodríguez (1997)).

Few concepts in the study of the molecular ISM have generated as much confusion as the interpretation that the near zero regression coefficient in the column density vs. size relationship implies that " $nL \sim \text{constant}$ " meaning that clouds of all sizes have the same average column density. The many follow-up studies, as evidenced by 2490 citations to Larson (1981), that include those seeking to verify, disprove, or improve, have not cleared up the confusion nor offered a satisfactory

TABLE 1 Log normal distributions of radius, column density, and line width

	radius, R (pc)	col. density, Σ (g cm^{-2})	line width, σ (km s^{-1})
log	0.56 ± 0.33	-1.97 ± 0.27	0.27 ± 0.22
linear	4.85 ± 4.29	0.013 ± 0.001	2.11 ± 1.1

TABLE 2 Comparison of Cloud Properties, Median Values

	radius (pc)	col. density (g cm^{-2})	Δv (km s^{-1})	$\langle \Delta v \rangle^1$ (km s^{-1})
This study	3.8	0.086	1.4	2.0
Rathborne et al. 2009	2.8	0.083	1.2	

¹ $\langle \Delta v \rangle$ indicates the mean of the velocity dispersions of all the pixels within the cloud radius, while Δv in this study derives from the single pixel of peak integrated intensity. In Rathborne et al (2009), Δv refers to the spectral FWHM defined by their segmentation algorithm and converted here to Gaussian width for comparison.

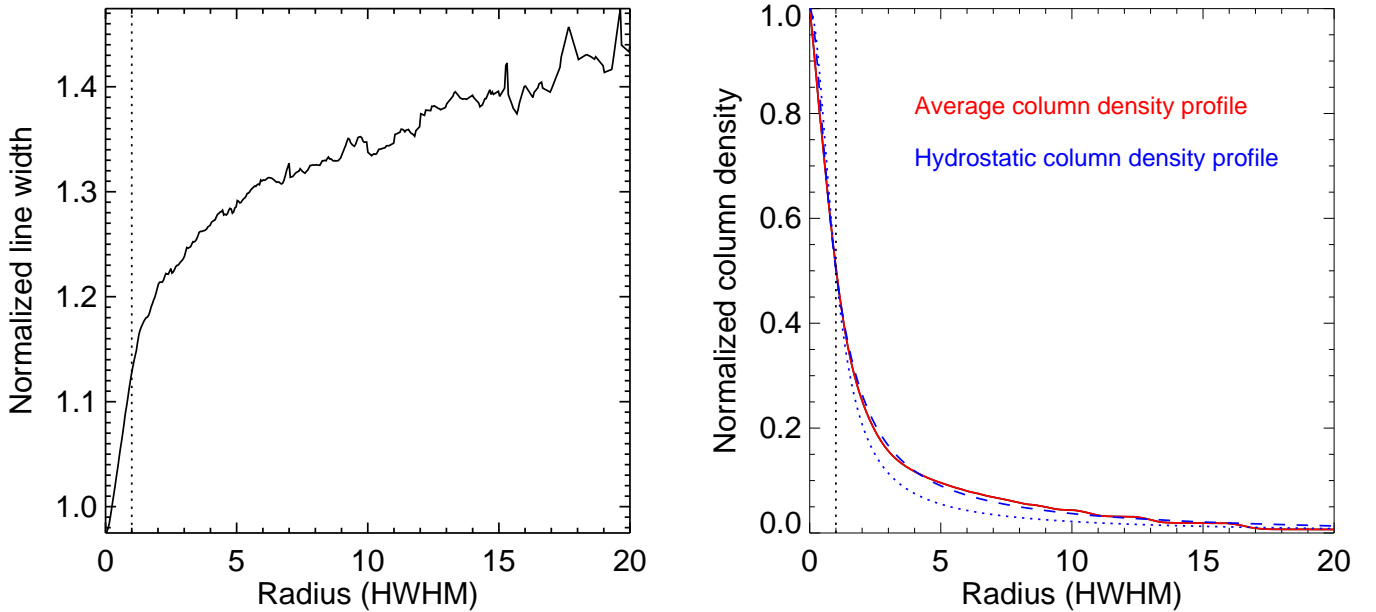


FIGURE 4 *Left*: Average non-dimensional line width profile of 3683 clouds (§3.3). *Right*: Average non-dimensional column density profile. In both figures, the vertical dashed line indicates $\text{HWHM} = 1$. The observed profile of column density is shown *right* as a red line. Two profiles of the column density in hydrostatic equilibrium are also shown (*right*) in blue with the dotted line for a non-dimensional isothermal temperature and the long-dashed line for a non-dimensional temperature proportional to the square of the line width (*left*).

explanation of the origin and implications of the two scalings. We return to this question after discussing our results of regressions of the properties of the GRS clouds.

4.6.1 | Correlations

Figure 7 shows the regressions of σ vs R and Σ vs R with the results listed in table 4. Because of the large sample size (4190

TABLE 3 Parameters of the 2-D Gaussian distribution of clouds, energy per unit mass

	GE (km^2s^{-2})	KE (km^2s^{-2})	GE (ergs cm^{-3})	KE (ergs cm^{-3})
log	1.01 ± 0.04	1.06 ± 0.04	-11.26 ± 0.57	-10.82 ± 0.57
linear	10.4 ± 1.01	11.5 ± 1.12	$1.31 \pm 2.85 \times 10^{-11}$	$3.53 \pm 7.69 \times 10^{-11}$

Quantities refer to the unrotated coordinates parallel to the axes of figure 5 , GE and KE.

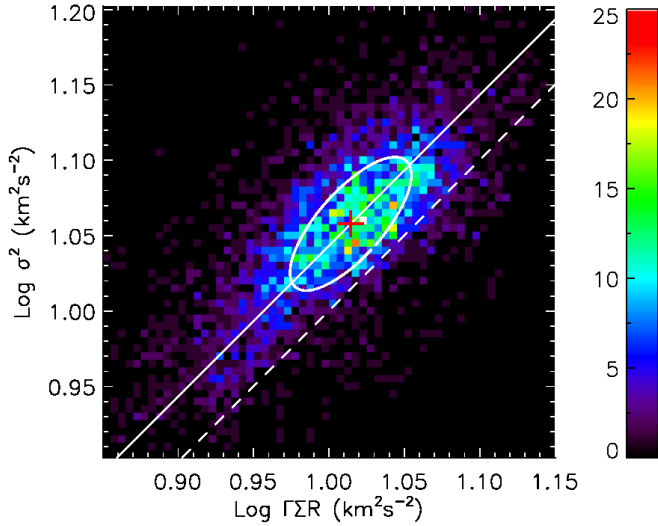


FIGURE 5 A 2-D histogram of the GRS clouds binned according to their gravitational potential energy (GE) and kinetic energy (KE) per unit mass with colors representing the number of clouds per bin of size $(0.05 \text{ km}^2\text{s}^{-2})^2$. The ellipse shows the standard deviations of the distribution from a 2-D Gaussian fit (table 3) with the mean marked with a cross. Constant pressure appears as a straight line in this space. The solid line identifies the average external pressure consistent with the three-term virial theorem (equation 1) and the mean GE and KE. The line of zero pressure is shown dashed.

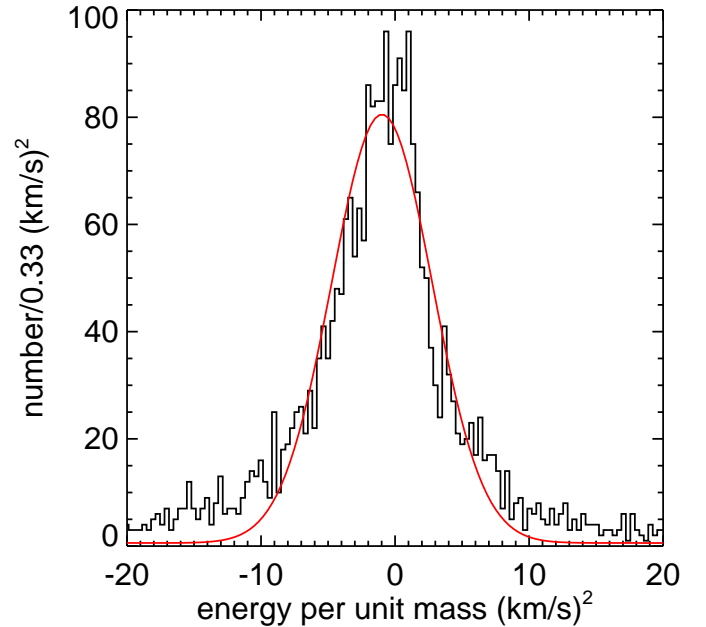


FIGURE 6 A 1-D histogram of the variable δ expressing the departure from time-dependent virial equilibrium from equation 1. The departures have a ragged normal distribution indicating that the measured mean $\delta = -0.97 \pm 3.76 \text{ (km}^2 \text{ s}^{-2})$ is consistent with time-dependent virial equilibrium.

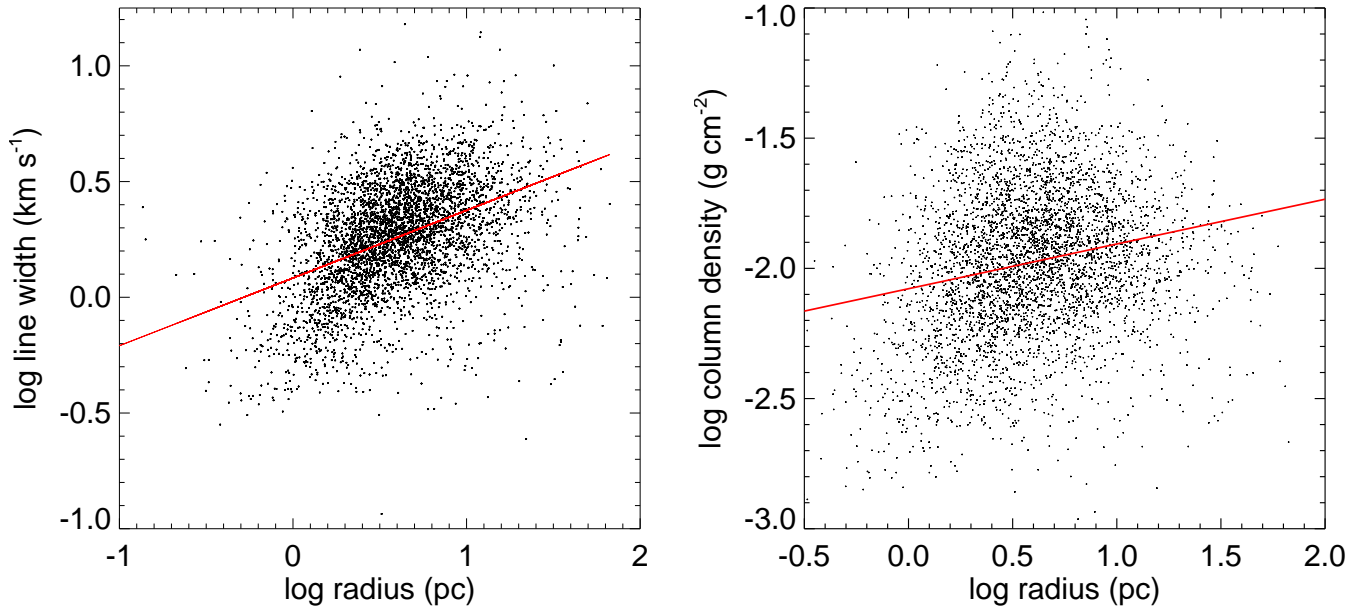
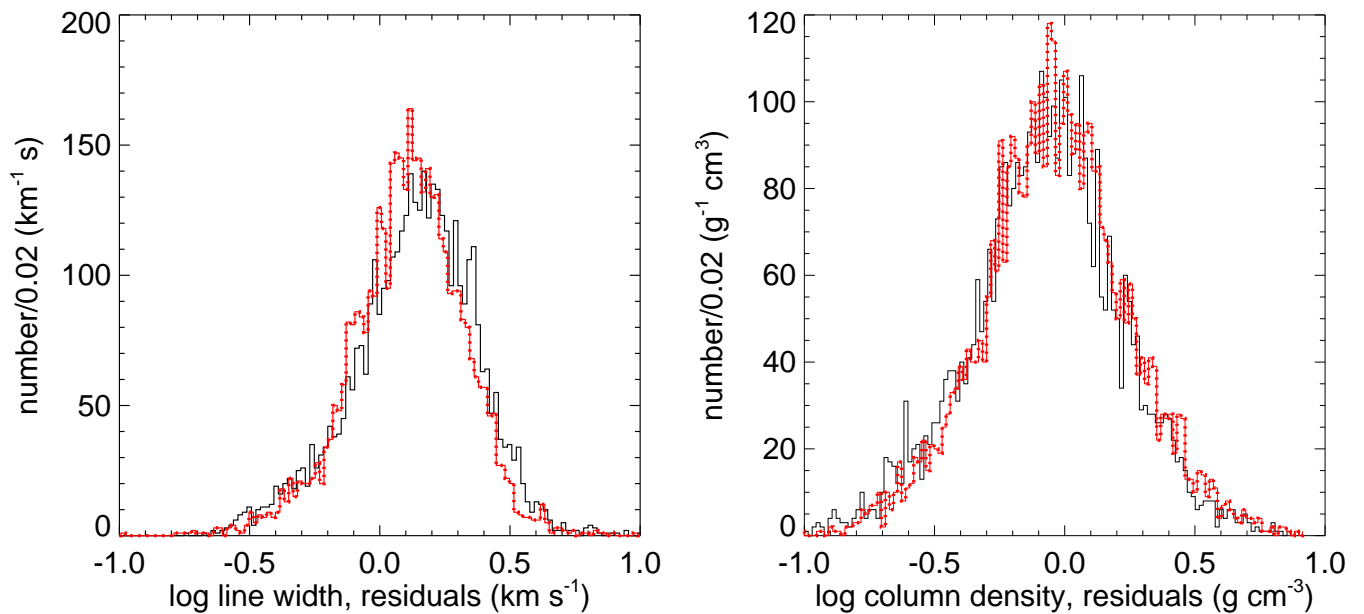
clouds), standard tests on the significance, p-value, F-test, or maximum likelihood, all find a vanishing small probability that these fits could arise by chance. Therefore, we evaluate the statistical significance by a different method.

The root mean square errors (RMSE) in both cases (table 4) are similar to the log standard deviations of the dependent variables (table 1). With Y as either of the dependent variables, σ or Σ , and $X = R$, the RMSE from the regression, $Y = b_0 + b_1 X_1$, is seen from the two tables to be essentially the same as the standard deviation of Y . Therefore, the expected value for the i th member of the sample, $\hat{Y}(i) = b_0 + b_1 X_1(i) \pm \text{RMSE}$, is no better estimate than the expected value of $Y(i)$ without the regression which is the mean of the sample $\mu_Y \pm \sigma_Y$ where σ_Y is the standard deviation of Y .

The point is demonstrated graphically in figure 8 which compares the distributions of the dependent variables, σ and Σ , with the distributions of their respective regression residuals. In both cases the distributions of the variable and the residuals are essentially the same. If a regression were significant, the mean of the residuals would shift left to a more negative number in the log space, and the width of the distribution (RMSE of the regression) would be narrower. Figure 8 (left, σ vs. R) shows a slight shift of the two distributions consistent with $\text{RMSE} < \sigma_\sigma$ although both equal 0.22 km s^{-1} . Because of the large sample size, the Kolmogoroff-Smirnov test for the equivalence of two distributions is inconclusive.

TABLE 4 Regressions

	Regression coeff. b	Std. err. σ_b	correlation coeff.	RMSE
σ vs. R	0.29 ($\text{km s}^{-1} \text{ pc}^{-1}$)	0.01 (km s^{-1})	0.71	0.22 (km s^{-1})
Σ vs. R	0.17 ($\text{g cm}^{-2} \text{ pc}^{-1}$)	0.01 (g cm^{-2})	0.21	0.28 (g cm^{-2})

**FIGURE 7** *Left*: Line width vs radius and *right*: column density vs radius both with regressions (solid red line).**FIGURE 8** Histograms of log line width *Left* and log column density *right* both with histograms of the regression residuals. The cloud properties are shown in black and the residuals in red with horizontal hash marks. The histograms of cloud properties are the same as in figure 2 . The residuals derive from the regressions in (figure 7).

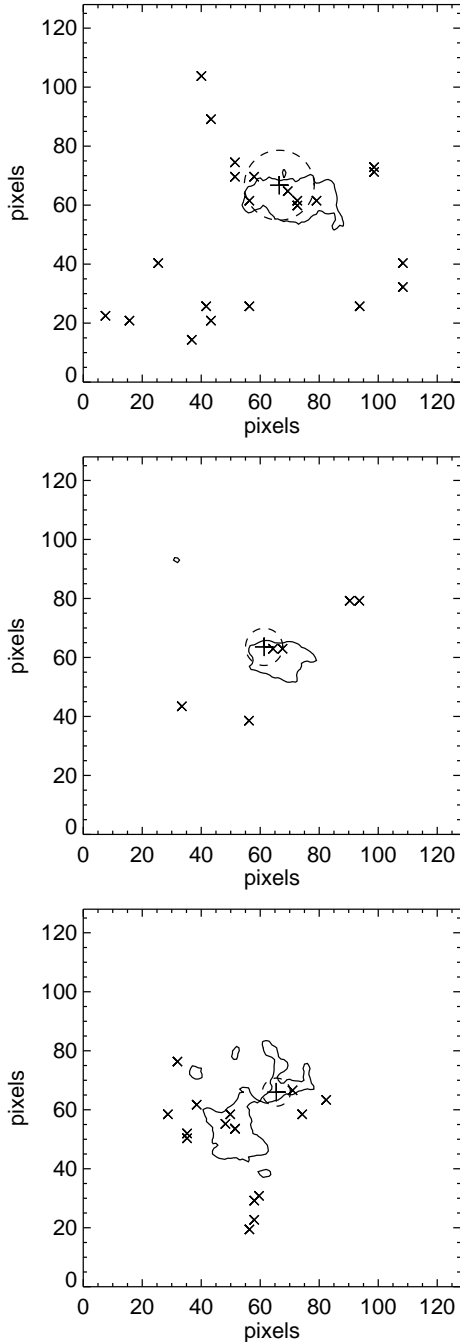


FIGURE 9 Contour maps of the ^{13}CO integrated intensity showing the complexity of cloud shapes. The single contour level is the half-power level of the cloud marked "+". The dashed circle shows the HWHM radius. Nearby clouds with similar VLSR are marked as "x". The examples *top* to *bottom* are clumps 5, 45, and 34 in Rathborne et al. (2009) with complexities of 1.5, 1.6, and 3.9, respectively.

4.6.2 | Uncorrelated or Constant Column Density

We return to the interpretation of a near zero value for the coefficient b_1 in the regression of Σ and R . If the dependent variable Σ were strictly constant aside from measurement errors, then Σ and R would be trivially uncorrelated. The interpretation of whether Σ is best described as constant or uncorrelated depends on the relative variances of Σ and R in the context of the physics under consideration, for example, virial equilibrium. Omitting the pressure term, equation (1) for virial equilibrium in terms of the energy per unit mass written in non-dimensional units is,

$$s^2 - rS = 0 \quad (2)$$

with these substitutions, $s = \sigma/\sigma_0$, $r = R/R_0$, and $S = \Gamma\Sigma R_0/\sigma_0^2$ for any σ_0 and R_0 , for example, $\sigma_0 = \mu_\sigma$ and $R_0 = \mu_R$. We find the non-dimensional standard deviations of s , r , $S = 0.88$, 0.54 , 0.15 . Since the standard deviations of the non-dimensional column density, S , and radius, r , are of the same order, the relationship between Σ and R is better described as uncorrelated. Constant might have been appropriate if the two were of different magnitudes such that the standard deviation of the non-dimensional GE, rS , were dominated by standard deviation of r . The observational evidence from the GRS clouds contradicts the interpretation that $b_1 \sim 0$ implies constant, average column density for clouds of all sizes.

4.6.3 | Autocorrelation

The correlation coefficient in regressions with one independent variable has a simple interpretation with zero indicating no correlation and a value of one indicating perfect correlation. The regression coefficient, b_1 , relating column density, Y , and radius, X_1 , can also be derived in a regression where $Y = n$, the number density (Larson, 1981), or $Y = M$ the mass (Lombardi, Alves, & Lada, 2010), as $b_{1,\Sigma} = b_{1,n} + 1$ or $b_{1,\Sigma} = b_{1,M} - 2$, respectively. However, in these regressions, the correlation coefficient always has a higher value closer to one because of the autocorrelation of n or M with radius.

Observationally, the mass is derived from sum of the ^{13}CO integrated intensities of all pixels within the cloud. Since each pixel represents an area, the autocorrelation of mass and radius is inherent.

The number density of molecular clouds cannot be derived in a simple way from observations of spectral line intensity because of the dependence of the intensity on the unknown path length through the cloud along the line of sight. The number densities in figure 5 of Larson (1981) that show a correlation with cloud size are derived from either the mass or column density reported by the observational studies cited and then by conversion by the appropriate power of R . The

apparent correlation in figure 5 of Larson (1981) is necessarily affected by autocorrelation.

4.6.4 | Other correlations

We find no interesting scaling relations in multiple regressions over a grid of variables other than the correlation between KE and GE (§4.4). Correlations that turned up were either due to autocorrelation or could be related back to the correlation of the energies. For example, in the scaling relationship suggested in Heyer et al. (2009), the variables σ^2/R and Σ are the KE and GE per unit volume after canceling a common factor of Σ .

4.7 | Complexity

Most of the GRS clouds have complex, non-circular shapes inconsistent with the 2-D projection of the 3-D spherical, minimum-energy configuration of hydrostatic equilibrium. Their shapes appear to be significantly affected by local turbulent fluctuations. We quantify the non-circular asymmetry with a complexity parameter defined as the ratio of the path length of the half-power contour around the peak integrated intensity to the circumference of a circle at the half-power radius. Figure 9 shows three example clouds with complexities of 1.5, 1.6 and 3.5. Although an elliptical cloud with a 2:1 axial ratio would have a complexity of 1.6, the examples in figure 9, (*left*) and (*middle*), show that cloud shapes with this complexity may already be more complex than elliptical. Also clouds with complex structure generally contain more than one cloud (or clump) shown as X's. The distribution of complexity is log normal, and 89% of the clouds have a complexity > 1.2 . The complexity is not correlated with any other cloud properties such as the ratio KE/GE.

4.8 | Column Density Probability Distribution Functions

Previous studies of low-mass star forming regions (Kainulainen, Beuther, Henning, & Plume, 2009) as well as some giant molecular clouds (Schneider et al., 2015) suggest that the column densities measured by infrared absorption have probability distribution functions (PDFs) that can be fit with a log normal at lower column densities and a power-law at higher column densities. The change in functional behavior is attributed to contraction of the clouds and star formation at the highest densities. This observational description is not so clear if the column densities are determined from molecular lines, even those that are typical tracers of high-density gas. In two studies (Schneider et al., 2016; Wang et al., 2020) column density PDFs from HCO⁺(1-0), HCN(1-0) HCN(1-0), and CS(2-1) in giant molecular clouds show power-law slopes at higher densities, those from ¹³CO(1-0) do not, while

the N₂H⁺(1-0) PDFs are inconsistent. Possible complications to the interpretation of PDFs based on molecular line observations include abundance variations due to chemistry and saturation of the spectral lines due to optical depth.

Although we lack star-formation tracers to identify contracting regions of the GRS clouds, we can compare column density PDFs from gas inside and outside of our 2 HWHM cloud boundaries. The PDFs of individual clouds are too noisy to be useful, so we resort to rescaling and averaging. Figure 10 shows the sample-average PDF of pixels within the clouds. The sample-average PDF outside the clouds is essentially the same and also consistent with a log normal distribution. This result is consistent with the two ¹³CO studies cited above.

However, a consideration of the completeness limit set by the observational noise allows a second interpretation of the PDF. We estimate the noise level in the sample average as $(2\langle\sigma_v\rangle/\Delta_v)^{1/2}\sigma_T$ where $\langle\sigma_v\rangle$ is the average velocity dispersion of the clouds, Δ_v is the spectral resolution, and σ_T is the observational noise in units of the antenna temperature. The estimated 3σ noise level is marked in figure 10 as a vertical line. The PDF could also be interpreted with a single power law that is fit to the distribution to the right of the completeness limit if the falloff in the number of clouds on the left side is due to incompleteness.

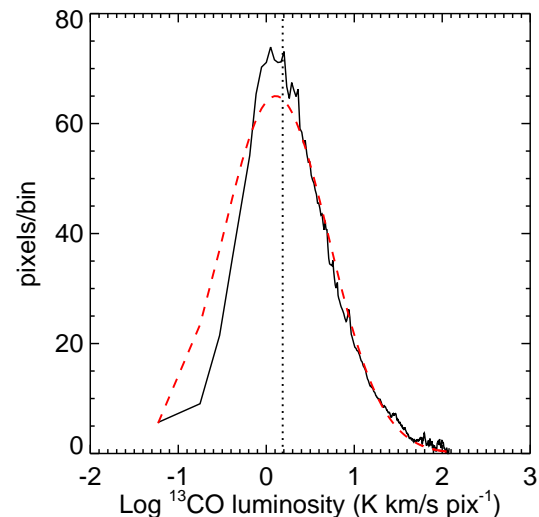


FIGURE 10 *Left*: Sample average column density PDF of the clouds on a log scale. The observational noise level is shown by the vertical, dotted line, and the best fit log normal Gaussian by the long-dashed line.

5 | DISCUSSION

The negative correlation of the ^{13}CO integrated intensity and spectral line width (§4.3) indicates a lower turbulent energy per unit mass at higher column densities. The explanation depends on which turbulent processes are responsible for the formation of molecular clouds.

If the clouds are formed by compression between turbulent flows, then the clouds could have lower line widths than the surrounding turbulence because the compressed regions are stagnation points with lower velocity dispersions (Klessen et al., 2005).

The explanation is different if the clouds are formed by the unstable growth of perturbations in energy due to a turbulent cooling instability (Keto et al., 2020). The scale-dependent cooling rate, σ/R , results in lower turbulent velocities on the smaller scales within the clouds and with respect to their surroundings.

However, there is a competing effect. Cooling, in combination with self-gravity and virialization, results in a negative heat capacity whereby the turbulent energy is rebalanced with the increased gravitational energy resulting from the contraction due to the loss of energy. Dissipation and contraction thus work at cross purposes with respect to the turbulent velocity dispersion.

The dissipation time scale and the dynamical time scale of the turbulence are both on the order of the crossing time, but different processes are involved, and the two need not be the same within a factor of order unity. The observed decrease in the turbulent velocity dispersion with spatial scale indicates that the turbulent dissipation time scale is shorter than the dynamical time scale that mediates the virialization. This difference in the two time scales allows perturbations to grow before they are erased by virialization. The turbulent molecular ISM described in this study is suitable for the turbulent cooling instability.

Clouds that contract to a critical density for dynamical stability with respect to a Jeans criterion either collapse to star formation or fragment into smaller clouds. The dispersion relation for the growth rate as a function of the dissipation rate indicates that fragmentation is preferred for faster rates of dissipation. The process is scale free and results in a fragmentation cascade as each newly formed fragment follows the same evolutionary path.

The fragmentation process cannot be followed by the analysis of a snapshot in time of the individual clouds, their surroundings, and their average properties. Analyzed differently, the GRS data may be helpful. A hierarchy of the GRS clouds is already suggested in the analysis by Rathborne et al. (2009). That study defines cloud complexes (their clouds) as associations of smaller clouds (their clumps) within a region

of similar Galactic coordinates and VLSR (l, b, VLSR). If this hierarchy represents two levels in a fragmentation cascade, some information on the fragmentation process may be gained from the study of the relationship of their clouds and clumps.

6 | CONCLUSIONS

We analyzed the ^{13}CO spectral line data of the GRS survey with new methods and provide new observational information on the properties of the turbulent molecular ISM that hold regardless of interpretation. However, in the absence of interpretation, the results showing hydrostatic and virial equilibrium appear paradoxical within a turbulent molecular ISM that is characterized by instability. The paradox can be resolved by consideration of the variation in the time scale for the evolution of turbulence at different spatial scales and consideration of the spatial scales of clouds within the surrounding molecular ISM.

Examination of Larson's scaling relations for column density and line width with radius finds neither correlation is significant. The inference of constant column density with cloud size is a misinterpretation of the lack of correlation.

6.1 | Observable properties of turbulence in the molecular ISM

The analysis of the GRS data provides specificity on the conditions of the turbulent molecular ISM. We identify both stationary and fluctuating properties. These observational properties should be useful for assessing theoretical models of turbulence in the molecular ISM

- 1) There is an overall average hydrostatic equilibrium across all scales in the turbulence. This is a stationary property that allows for local fluctuations and does not require any region to be in hydrostatic equilibrium.
- 2) Regions with higher column density have lower spectral line widths and lower turbulent kinetic energy per unit mass.
- 3) The kinetic and gravitational energies within a cloud are virialized with a ratio set by the local pressure energy around each cloud. The three energies are fluctuating components of the turbulence.
- 4) The ratio of the mean kinetic and gravitational energies per unit mass within clouds is $\langle 2KE \rangle / \langle GE \rangle \sim 2.2$.
- 5) The average excess kinetic energy interpreted as a pressure (energy per unit volume) is comparable to the average pressure of the multiphase ISM at the Galactic mid-plane. This is a stationary property of the turbulence. The mid-plane pressure of the Galaxy may be a boundary condition for the molecular phase of the turbulence.

REFERENCES

- Ballesteros-Paredes, J., Román-Zúñiga, C., Salomé, Q., Zamora-Avilés, M., & Jiménez-Donaire, M. J. (2019), *MNRAS*, *490*, 2648-2655.
- Bloemen, J. B. G. M. (1987), *ApJ*, *322*, 694.
- Boulares, A., & Cox, D. P. (1990), *ApJ*, *365*, 544.
- Elmegreen, B. G. (1989), *ApJ*, *338*, 178.
- Elmegreen, B. G. (1993), *ApJ*, *419*, L29.
- Evans, I., Neal J., Heyer, M., Miville-Deschênes, M.-A., Nguyen-Luong, Q., & Merello, M. (2021), *ApJ*, *920*, 126.
- Field, G. B., Blackman, E. G., & Keto, E. R. (2011), *MNRAS*, *416*, 710-714.
- Gammie, C. F., & Ostriker, E. C. (1996), *ApJ*, *466*, 814.
- Heyer, M., Krawczyk, C., Duval, J., & Jackson, J. M. (2009), *ApJ*, *699*, 1092-1103.
- Jackson, J. M., Rathborne, J. M., Shah, R. Y. et al. (2006), *ApJS*, *163*, 145-159.
- Kainulainen, J., Beuther, H., Henning, T., & Plume, R. (2009), *A&A*, *508*, L35-L38.
- Keto, E., Field, G. B., & Blackman, E. G. (2020), *MNRAS*, *492*, 5870-5877.
- Klessen, R. S., Ballesteros-Paredes, J., Vázquez-Semadeni, E., & Durán-Rojas, C. (2005), *ApJ*, *620*, 786-794.
- Kolmogorov, A. N. (1941), *Akademiia Nauk SSSR Doklady*, *32*, 16.
- Kritsuk, A. G., Lee, C. T., & Norman, M. L. (2013), *MNRAS*, *436*, 3247-3261.
- Larson, R. B. (1981), *MNRAS*, *194*, 809-826.
- Lombardi, M., Alves, J., & Lada, C. J. (2010), *A&A*, *519*, L7.
- Mac Low, M.-M., & Klessen, R. S. (2004), *Reviews of Modern Physics*, *76*, 125-194.
- Miville-Deschênes, M.-A., Murray, N., & Lee, E. J. (2017), *ApJ*, *834*, 57.
- Padoan, P. (1995), *MNRAS*, *277*, 377-388.
- Phiri, S. P., Kirk, J. M., Ward-Thompson, D., Sansom, A. E., & Bendo, G. J. (2021), *MNRAS*, *504*, 4511-4521.
- Rathborne, J. M., Johnson, A. M., Jackson, J. M., Shah, R. Y., & Simon, R. (2009), *ApJS*, *182*, 131-142.
- Roman-Duval, J., Jackson, J. M., Heyer, M., Johnson, A., Rathborne, J., Shah, R., & Simon, R. (2009), *ApJ*, *699*, 1153-1170.
- Roman-Duval, J., Jackson, J. M., Heyer, M., Rathborne, J., & Simon, R. (2010), *ApJ*, *723*, 492-507.
- Scalo, J. (1990), Perception of interstellar structure - Facing complexity. In R. Capuzzo-Dolcetta, C. Chiosi, & A. di Fazio (Eds.), *Physical Processes in Fragmentation and Star Formation* Vol. 162, p. 151-176.
- Schneider, N., Bontemps, S., Girichidis, P. et al. (2015), *MNRAS*, *453*, L41-L45.
- Schneider, N., Bontemps, S., Motte, F. et al. (2016), *A&A*, *587*, A74.
- Solomon, P. M., Rivolo, A. R., Barrett, J., & Yahil, A. (1987), *ApJ*, *319*, 730.
- Spitzer, L. 1978, *Physical processes in the interstellar medium*.
- Vázquez-Semadeni, E. (1998), *arXiv e-prints*, astro-ph/9810380.
- Vázquez-Semadeni, E., Ballesteros-Paredes, J., & Rodríguez, L. F. (1997), *ApJ*, *474*, 292-307.
- Wang, Y., Beuther, H., Schneider, N. et al. (2020), *A&A*, *641*, A53.

7 | SUPPORTING INFORMATION

Some results of this analysis are available on the Harvard Dataverse: Keto, Eric, 2024, "Replication Data for: Scales of Stability and Turbulence in the Molecular ISM", <https://doi.org/10.7910/DVN/5Y0C4E>, Harvard Dataverse, V1 These additional data include a catalog of the cloud properties such as radius, velocity dispersions, column densities, and mass. The additional data also include the azimuthally-averaged radial profiles of line width and column density as well as the PDFs of the pixels within and outside the cloud boundaries.

